J. Fluid Mech. (1998), *vol.* 362, *pp.* 327–346. Printed in the United Kingdom

Shock cavity implosion morphologies and vortical projectile generation in axisymmetric shock–spherical fast/slow bubble interactions

By N. J. ZABUSKY AND S. M. ZENG

Department of Mechanical and Aerospace Engineering,
Rutgers University, Piscataway, NJ 08854-8058, USA
e-mail: nzabusky@caip.rutgers.edu

(Received 30 September 1996 and in revised form 26 September 1997)

Collapsing shock-bounded cavities in fast/slow (F/S) spherical and near-spherical configurations give rise to expelled jets and vortex rings. In this paper, we simulate with the Euler equations planar shocks interacting with an R12 axisymmetric spherical bubble. We visualize and quantify results that show evolving upstream and downstream complex wave patterns and emphasize the appearance of vortex rings. We examine how the magnitude of these structures scales with Mach number. The collapsing shock cavity within the bubble causes secondary shock refractions on the interface and an expelled weak jet at low Mach number. At higher Mach numbers (e.g. $M = 2.5$) 'vortical projectiles' (VP) appear on the downstream side of the bubble. The primary VP arises from the delayed conical vortex layer generated at the Mach disk which forms as a result of the interaction of the curved incoming shock waves that collide on the downstream side of the bubble. These rings grow in a self-similar manner and their circulation is a function of the incoming shock Mach number. At $M = 5.0$, it is of the same order of magnitude as the primary negative circulation deposited on the bubble interface. Also at $M = 2.5$ and 5.0 a double vortex layer arises near the apex of the bubble and moves off the interface. It evolves into a VP, an asymmetric diffuse double ring, and moves radially beyond the apex of the bubble. Our simulations of the Euler equations were done with a second-order-accurate Harten–Yee-type upwind TVD scheme with an approximate Riemann Solver on mesh resolution of 803×123 with a bubble of radius 55 zones.

1. Introduction

Phenomena in shock-accelerated gas flows arise in laser-induced ('inertial confinement') fusion, supersonic combustion and supernova astrophysics.

The shock–gas bubble interaction was first studied experimentally by Rudinger & Sommers (1960). About ten years ago Haas & Sturtevant (1987) investigated experimentally shock–cylinder and shock–sphere interactions at low Mach number for both the fast/slow (F/S) and slow/fast (S/F) case to examine the nature of shock refractions. For the spheres, let us scrutinize what they observed and reported concerning vortex related phenomena.

For a He spherical bubble in air at $M = 1.25$ (figure 8*e* at 350 μs) 'The air jet impinges on the downstream He–air interface and pierces it'. 'Forming a more distinct vortex ring than in the cylindrical case.... The small scales evident on the vortex ring at later times... indicate that it contains most of the vorticity in the flow and is the region in which the most intense mixing takes place.' Later they say, 'Concentrated vorticity also occurs along the conical shear layer at the boundary of the reentrant jet in the main body...'.

For R22 in air at $M = 1.25$ (figure 14 at 507 μs.) 'it is seen that the deformation of the wedge created by the transmitted wave near its focus, ultimately forming a narrow axial jet, is much more extreme than in the cylindrical case, presumably because of the stronger focus in axial symmetry. On the other hand, the surrounding vortex, which in the cylindrical case is a vortex pair, is much more diffuse.' They also note that the hanging bubble is an 'oval' and hence not perfectly axisymmetric.

In the experiments, images were provided as single shadowgraphs per run. Since shadowgraphs provide density fluctuation information, they do not give a quantitative discussion of vorticity but only a broad view. In particular, they do not indicate any of the following:

(*a*) The generation of secondary (opposite-signed) vorticity in the region where the incoming shock intersects the density-stratified interface.

(*b*) The intensification of pressure and temperature within the internal imploding cavity.

(*c*) The mechanism of axial 'jet-ring' formation after the imploding cavity is focused to its smallest volume or after the incoming shock ceases contact with the downstream side of the heavier bubble.

(*d*) The emergence of vortical projectiles.

Early axisymmetric simulations were made by Picone & Boris (1988) (for $M = 1.25$ and air/Freon-22) and by Cowperthwaite (1992) (for $M = 1.12$ and air/Freon-12). Some of the above enumerated phenomena were revealed in the high resolution axisymmetric simulations by Winkler *et al.* (1987) and recently in the high-resolution simulations of interstellar clouds by Klein, Mckee & Colella (1994). However, the causative effects and the scaling of phenomena were not presented and will be given below. Samtaney & Zabusky (1993, 1994), using a local shock polar analysis, proposed models for the circulation deposited in two-dimensional shock–interface interactions, including cylinders.

In this paper we examine with inviscid codes at Mach numbers up to $M = 5$ the behaviour at *early times*, when the shock is passing over the bubble and primary vorticity is deposited on the bubble interface, and at *intermediate times*, when the incident shock is no longer in contact with the bubble and the transmitted shock wave forms an internal cavity which implodes into a small focal domain.

During the intermediate time interval the deposited negative vorticity continues to roll up and, at higher Mach numbers, separates from the interface. Also, the incident shock has been curved by passing over the bubble and interacts with itself on the downstream side of the bubble and generates a Mach disk and conical vortex layers which roll up into vortex rings, which have a self-similar character and can be supersonic. We have also found something new and significant that is revealed clearly at $M = 5$, namely double vortex rings form on the top or near the apex of the bubble. For all the Mach numbers examined the bubble is sheared into small-scale structures. We believe that at late times a proper study of mixing will require the use of much higher resolution codes. During these time periods the processes of

wave reflection, refraction, and focusing inside or outside a bubble all play important roles.

2. Equations of motion and numerical method for multi-species flow

2.1. *Basic equations*

We use a shock-capturing numerical method to solve the compressible Euler equations in a two-dimensional axisymmetric *two species* representation. The gases are assumed to be inviscid, perfect and in thermal equilibrium with no chemical reactions between species. The basic equations of the conservation of mass, momentum and energy in the generalized coordinate system can be written in a concise form as

$$\hat{\boldsymbol{U}}_t + \hat{\boldsymbol{F}}_\xi + \hat{\boldsymbol{G}}_\eta + \hat{\boldsymbol{W}} = 0, \tag{1}$$

where

$$(\hat{\boldsymbol{U}}, \hat{\boldsymbol{F}}, \hat{\boldsymbol{G}}, \hat{\boldsymbol{W}}) = \frac{1}{J}(\boldsymbol{U}, \xi_x \boldsymbol{F} + \xi_r \boldsymbol{G}, \eta_x \boldsymbol{F} + \eta_r \boldsymbol{G}, \boldsymbol{W}), \tag{2}$$

where the Jacobian of transformation

$$J = \xi_x \eta_r + \eta_x \xi_r. \tag{3}$$

Here, $\boldsymbol{U} = [\rho_1, \rho_2, \rho u, \rho v, E]^T$, $\boldsymbol{F} = [\rho_1 u, \rho_2 u, \rho u^2 + p, \rho uv, (E+p)u]^T$, $\boldsymbol{G} = [\rho_1 v, \rho_2 v, \rho uv, \rho v^2 + p, (E+p)v]^T$, and $\boldsymbol{W} = (1/r)[\rho_1 u, \rho_2 u, \rho u^2, \rho uv, (E+p)u]^T$. In the above equations, t, x and r indicate time, and the space co-ordinates in horizontal and radial directions, ρ, p, E, u, and v are the density, the pressure, the total energy per unit volume and velocity in the x- and r-directions, respectively.

The system is closed by a perfect gas equation of state

$$p = (\gamma - 1)\rho e = (\gamma - 1)\left[E - \frac{\rho}{2}\left(u^2 + v^2\right)\right], \tag{4}$$

where

$$p = \rho_1 R_1 T + \rho_2 R_2 T = \left(\frac{\rho_1}{m_1} + \frac{\rho_2}{m_2}\right) RT. \tag{5}$$

Here T is the temperature, m_i is the molecular weight, R_i is the gas constant, and γ_i is the specific heat ratio for both ambient and bubble gases. Subscripts 1 and 2 indicate ambient and the bubble gas, e.g. air and R12, respectively.

From the above we can show that

$$p = \{\gamma_1 z_1 + \gamma_2 z_2 - 1\}\, \rho e, \tag{6}$$

or in regions where the gases interdiffuse the effective specific heat ratio is given by the interpolation

$$\gamma = \gamma_1 z_1 + \gamma_2 z_2 \tag{7}$$

where

$$z_i = \frac{\rho_i / [m_i(\gamma_i - 1)]}{\dfrac{\rho_1}{m_1(\gamma_1 - 1)} + \dfrac{\rho_2}{m_2(\gamma_2 - 1)}}.$$

The local sound speed is defined by $c^2 = (\gamma p/\rho)$.

2.2. *Boundary conditions*

The computational domain considered in the present work is illustrated in figure 1, where the base flow field consists of a spherical bubble region and an ambient air

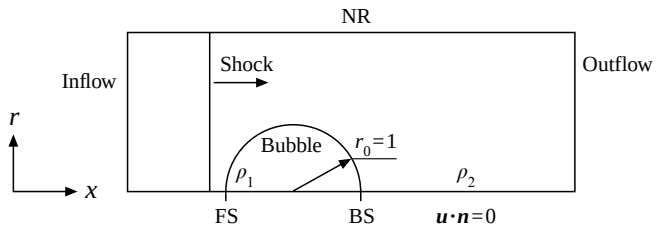

FIGURE 1. Schematic of axisymmetric computational domain and boundary conditions. Boundaries are inflow/outflow (i.e. non-reflective, NR) or relective, $\boldsymbol{u}\cdot\boldsymbol{n}=0$. The bubble interfaces are designated: FS, for front side (or upstream); or BS, back side (or downstream).

region. The boundary may be arbitrary and is described by unit tangent and normal vectors $\boldsymbol{l}$ and $\boldsymbol{n}$, where

$$\boldsymbol{l}\cdot\boldsymbol{n}=0. \tag{8}$$

For axisymmety, the boundary condition is

$$\boldsymbol{u}\cdot\boldsymbol{n}=0, \tag{9}$$

$$\frac{\partial(\boldsymbol{u}\cdot\boldsymbol{l})}{\partial\boldsymbol{n}}=0, \tag{10}$$

where $\boldsymbol{u}=(u,v)^T$ is the velocity. Only (9) is applied on the axis. Equation (10) denotes that the shear stress equals zero on the boundary interface.

For the inflow and outflow boundaries in figure 1, we utilize the multidimensional compatibility relations (Hirsch 1992) for the momentum equation

$$\boldsymbol{n}\cdot\mathrm{D}_{t\pm}\boldsymbol{u}\pm\frac{1}{\rho c}\mathrm{D}_{t\pm}p\pm c[\nabla\cdot\boldsymbol{u}-\boldsymbol{n}\cdot(\boldsymbol{n}\cdot\nabla)\boldsymbol{u}]=0, \tag{11}$$

where

$$\mathrm{D}_{t\pm}=\frac{\partial}{\partial t}+(\boldsymbol{u}\pm c\boldsymbol{n})\cdot\nabla, \tag{12}$$

indicates the derivative along the bicharacteristics ($\boldsymbol{u}\pm c\boldsymbol{n}$). In this compatibility relation, the first two terms correspond exactly to the one-dimensional Riemann variables, but are written for the velocity component in direction $\boldsymbol{n}$. The compatibility relation for constant $\boldsymbol{n}$ leads to the following expression:

$$\mathrm{D}_{t\pm}R_n^{\pm}=\mp c\boldsymbol{n}\cdot(\boldsymbol{n}\cdot\nabla)\boldsymbol{u}. \tag{13}$$

The Riemann variables $R_n^{\pm}$ associated with the direction $\boldsymbol{n}$ for an isentropic flow are defined by

$$R_n^{\pm}=\boldsymbol{u}\cdot\boldsymbol{n}\pm\frac{2c}{\gamma-1}. \tag{14}$$

As in the one-dimensional case, let us assume that the pressure and the velocity are uniform on the boundary surface, and that the flow is isentropic. According to (13), the Riemann variables R_n^{+} and R_n^{-} are now constants along the slopes $\boldsymbol{u}+c\boldsymbol{n}$ and $\boldsymbol{u}-c\boldsymbol{n}$. Equation (14) corresponds to the incoming and outgoing characteristics. Thus, the compatibility relations at the boundary can be written as

$$R_B^{+}=u_B+\frac{2c_B}{\gamma-1}=u_L+\frac{2c_L}{\gamma-1}, \tag{15}$$

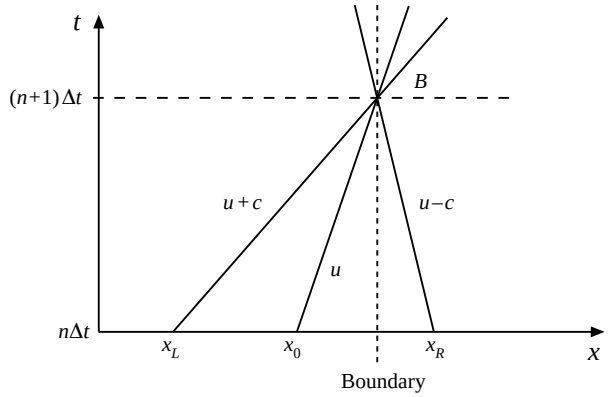

FIGURE 2. Schematic illustration of the inflow boundary condition.

Gas	Molecular weight	Gas constant R (J kg^{-1} K^{-1})	Specific heat γ	Speed of sound c (m s^{-1})
Air	28.96	287.1	1.402	343
R12	120.9	68.8	1.141	152

TABLE 1. Interface parameters

$$R_B^- = u_B - \frac{2c_B}{\gamma - 1} = u_R - \frac{2c_R}{\gamma - 1}, \tag{16}$$

where the subscript B, L and R indicate the value at the boundary, $x = x_L$ and $x = x_R$, respectively. x_R is an internal mesh point, and its values are obtained as the solution at $t = n\Delta t$ by an appropriate extrapolation at the mesh point close to the boundary. The value at $x = x_L$ is the free-stream value, which is given as a physical boundary condition. The schematic illustration of the inflow boundary condition is shown in figure 2.

The boundary values of the normal velocity u_B and speed of sound c_B are obtained by adding and subtracting equations (15) and (16) leading to

$$u_B = \frac{R_B{}^+ + R_B{}^-}{2}, \tag{17}$$

$$c_B = \left(R_B{}^+ - R_B{}^-\right) \frac{\gamma - 1}{4}. \tag{18}$$

This method is easily generalized to many fluid species and complex boundaries in three dimensions.

2.3. *Initial conditions and normalization*

We use a dense spherical bubble of R12 whose ambient parameters are in table 1. The density initial ratio $\eta = 4.17$ and the initial air pressure/density ratio is $p_0/\rho_0 = RT_0$ where $T_0 = 293$ k.

We drive the system with a plane shock wave of Mach numbers 1.14, 1.5, 2.5 and 5.0. The first case we consider is the weak shock and corresponds to the experiment by Philpott *et al.* (1992).

The mesh resolution is 803×123 zones and the radius of the bubble is 55 zones.

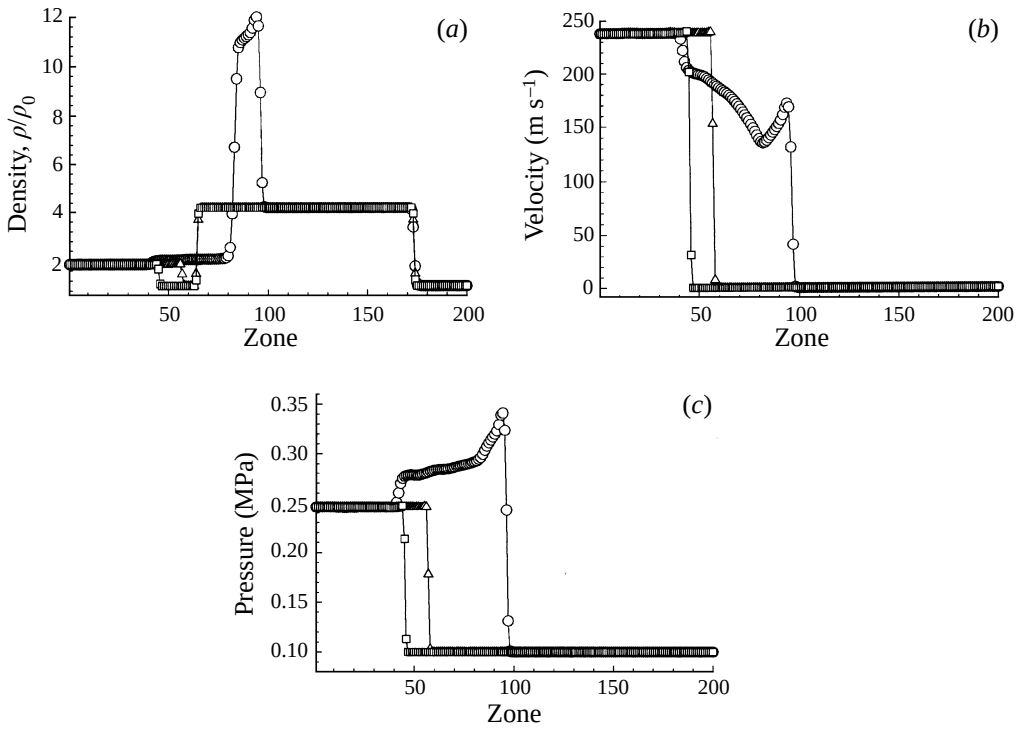

FIGURE 3. Density, velocity and pressure distribution along the x-axis in a shock-bubble interaction. $M = 1.5$, air–R12 bubble of radius 55 zones: –○–○–○–, $t = 1.7 \times 10^{-4}$; –△–△–, $t = 5.1 \times 10^{-4}$; –□–□–, $t = 2.5 \times 10^{-3}$.

At $t = 0$ the shock is 20 zones to the left of the bubble. As shown in figure 3, a Mach 1.50 shock translates 13 zones in four time steps. The size of a time step is determined from the CFL condition. Initially, the thickness of the shock front and bubble interface are each two zones. Time is normalized as tM (where M is the Mach number) and distance by the bubble radius r_0. Note, it takes 0.0025 normalized time units for a shock to translate a distance r_0 in air.

2.4. *Numerical methods*

Shock wave refraction at a gaseous interface is normally accompanied by wave propagation, reflection and diffraction. Under these conditions, the numerical simulation becomes rather complicated and difficult. Among the several formal concepts proposed in the literature to treat the weak solution problem, we select a scheme that suppresses spurious oscillations. A Harten–Yee second-order-accurate, upwind finite-difference scheme (Harten 1993; Yee, Warming & Harten 1985) based on the TVD (total variation diminishing) algorithm was applied to equations (1) to (4) and (7). The key idea is to evaluate the fluxes of mass, momentum and energy from solutions to TVDs that arise at each cell interface. Here we present only a brief description of the algorithm.

An operator splitting is performed on equation (1), whereby the two-dimensional axisymmetric equations are split into sets of three one-dimensional equations. The splitting is represented by the one-dimensional operators, L_ξ, L_η, L_s as follows:

for L_ξ by

$$\hat{\boldsymbol{U}}_t + \hat{\boldsymbol{F}}_\xi = 0,$$

for L_η by

$$\hat{\boldsymbol{U}}_t + \hat{\boldsymbol{G}}_\eta = 0.$$

for L_s by

$$\hat{\boldsymbol{U}}_t + \hat{\boldsymbol{W}} = 0.$$

Thus, (1) can be written as

$$\hat{\boldsymbol{U}}_{i,j}^{n+2} = L_\xi L_\eta L_s L_s L_\eta L_\xi \hat{\boldsymbol{U}}_{i,j}^{n}, \tag{19}$$

where $\hat{\boldsymbol{U}}_{i,j}^{n} = \hat{\boldsymbol{U}}(n\Delta t, i\Delta\xi, j\Delta\eta)$, superscript n is the time level, and subscripts i and j are the coordinates of the mesh. For the source term, $\hat{\boldsymbol{W}}$, the operator, $L_s\hat{\boldsymbol{U}}_{i,j}^{\mathrm{n}}$ is calculated by the secondary-order Runge–Kutta integration. The finite-difference operator for L_ξ is given by

$$\hat{\boldsymbol{U}}_{i,j}^{*} = L_\xi \hat{\boldsymbol{U}}_{i,j}^{\mathrm{n}} = \hat{\boldsymbol{U}}_{i,j}^{\mathrm{n}} - \frac{\Delta t}{\Delta\xi}[\hat{\boldsymbol{F}}_{i+1/2,j}^{n} - \hat{\boldsymbol{F}}_{i-1/2,j}^{n}]. \tag{20}$$

An approximate Riemann solver, developed by Roe (1981, 1983) is used in the scheme. It is based on a characteristic decomposition of the flux differences while ensuring the conservation properties of the scheme. According to this solver, the flux $\hat{\boldsymbol{F}}_{i+1/2}$ is

$$\hat{\boldsymbol{F}}_{i+1/2,j} = \tfrac{1}{2}\left(\hat{\boldsymbol{F}}_{i+1,j} + \hat{\boldsymbol{F}}_{i,j} + \boldsymbol{R}_{i+1/2}\Phi_{i+1/2}\right), \tag{21}$$

where $\boldsymbol{R}_{i+1/2}$ is the right-hand eigenvector of the Jacobian matrix, and Φ is the modified flux vector. To obtain the flux $\hat{\boldsymbol{G}}$ for L_η, we use an equation similar to (21).

2.5. *Visiometric methods*

As described in Bitz & Zabusky (1990), we visualize and quantify the scalars: density, ρ; dilatation, div $\boldsymbol{u}$ (to highlight wavefronts and shock waves); vorticity, ω,

$$\omega = \boldsymbol{e}_\phi \cdot \nabla \times \boldsymbol{u}, \tag{22}$$

and the numerical shadowgraph, $\Delta\rho$ (to juxtapose contact discontinuities and shock fronts). Here, $\boldsymbol{e}_\phi$ represents the azimuthal unit vector normal to the plane of the calculation. The Laplacian may oscillate in space and so is reserved for early time analysis.

To obtain a global view of the flow we project the solution to a lower dimensions by presenting space–time diagrams of integrated vorticity and positive vorticity as well as the pressure on the axis. The integrated positive and negative vorticity can be written

$$\gamma_\pm(x,t) = \int \omega_\pm(x,r,t)\mathrm{d}r. \tag{23}$$

The domain of integration is chosen to highlight specific phenomena. For example, to examine the negative circulation on the interface and within the bubble we accumulate only those cells with $\omega_- < 0$ that coincide with the location of ρ_2, the bubble fluid. Similarity, we accumulate all $\omega_+ > 0$ to examine secondary vortex process. These arise from 'baroclinic' processes in the equation

$$\frac{\mathrm{D}\omega}{\mathrm{D}t} = \frac{1}{\rho^2}\nabla\rho \times \nabla p - \omega(\nabla \cdot \boldsymbol{u}) + (\omega \cdot \nabla)\boldsymbol{u}. \tag{24}$$

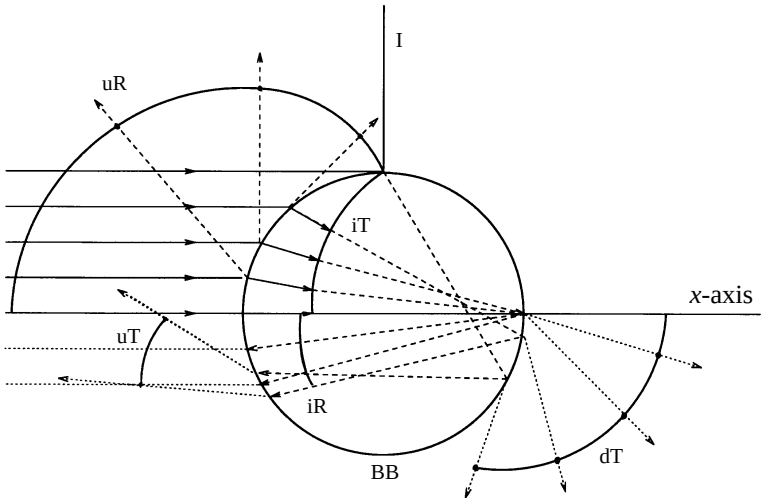

FIGURE 4. Schematic illustration of rays and wave fronts at various times for a F/S gaseous bubble interface: BB, bubble interface; uR, upstream reflected; iT, interior transmitted; iR, interior reflected; dT, downstream transmitted; uT, upstream transmitted. The bubble boundary and wavefronts are solid lines. The rays after iT are dashed lines.

In two-dimensions the last term is omitted and we find that the second, or dilatation term, plays a small role for the parameter range and time intervals being considered. The dominant primary vorticity arises from the first, or baroclinic, term. A layer of vorticity is generated due to the misalignment of the local pressure and density gradients. Roughly, for F/S, a negative layer is deposited because the pressure gradient is associated with the shock and is in the $-x$ direction while the density gradient is in the radial direction. Another source of vorticity is the developing curvature of shocks or the interaction of shocks, e.g. which arises at a Mach disk on the downstream side of the bubble.

3. Results and discussion

3.1. *Wave patterns and correlation with vortex deposition*

To help interpret phenomena, particularly complex shock wave patterns, we present the geometric acoustical ray and wave front diagram for a heavy (e.g. R12) bubble in air in figure 4. For this strongly convergent lens, we see: incident planar (I) and upstream reflected curved (uR) rays and wavefronts; a transmitted curved wavefront in the bubble (iT); and curved wavefronts transmitted from the bubble to the outer upstream and downstream sides (uT and dT). Snell's Law describes the refraction angles and can be written as

$$n = \frac{\sin\theta_i}{\sin\theta_r} = \frac{c_1}{c_2}, \tag{25}$$

where, θ_i and θ_r are the angles of the incident and refraction rays and c_1 and c_2 are the speeds of sound in the fast and slow mediums.

When a planar shock wave collides with an oblique gaseous interface, it refracts over it either as a regular refraction (RR) or an irregular refraction (IR). This depends on the local angle of the incident shock, α_i, the Mach number of the incident shock wave, M, as well as the characteristic parameters of the gases, such as densities and specific heat ratio. All types of configurations, from RR to IR, will appear as the

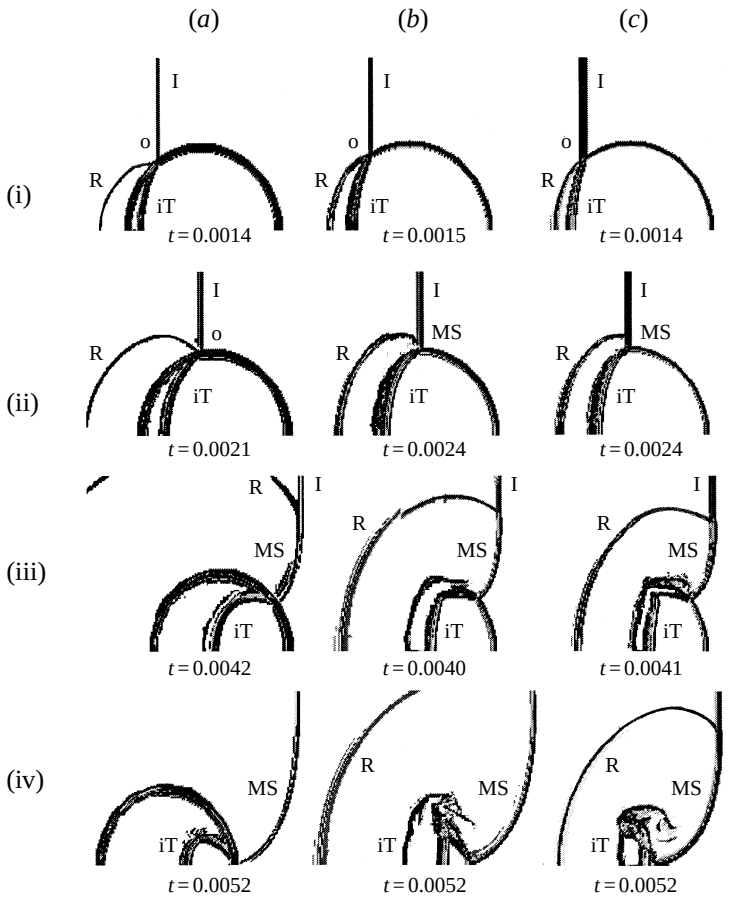

FIGURE 5. Numerical shadowgraph, $\Delta\rho$, for shock refraction on an air–R12 bubble in cases (*a*) $M = 1.14$, (*b*) $M = 2.5$ and (*c*) $M = 5.0$. Time is normalized as tM (where M is the Mach number) and distance by the bubble radius, r_0. Note, it takes 0.0025 normalized time units for a shock to cross r_0 in air.

shock crosses over the interface. Our investigation shows that the configurations of the shock refraction have an important effect on vorticity generation. The complexity of the interaction of a shock with a heavy spherical bubble varies with time.

The 'early' phase begins at the time of initial contact of the incident planar shock waves with the back (upstream) side of the bubble and lasts until the time of last contact with the front (downstream) side of the bubble. This phase is divided into four subphases as shown in the numerical shadowgraphs of figure 5. Just after the incident shock impinges on the spherical bubble interface all three shock waves, I, uR and iT, meet at a node, o, that is we have a regular reflection (conventionally designated as RR in Ben Dor 1992), as shown in row 1.

In the second row, when the incident shock is near or at the apex of the bubble, two types of refraction are indicated: in (*a*)(i) for $M = 1.14$ we have regular reflection with a reflected expansion wave but in (*b*)(ii) and (*c*)(ii) (for $M = 2.5$ and $M = 5.0$) we have a Mach reflection type of refraction (MR) in which a Mach stem, Ms, arises on the interface. The configuration of MR remains for all the following times. Note that the triple point (downstream end of the reflected shock) is moving vertically along the incident shock.

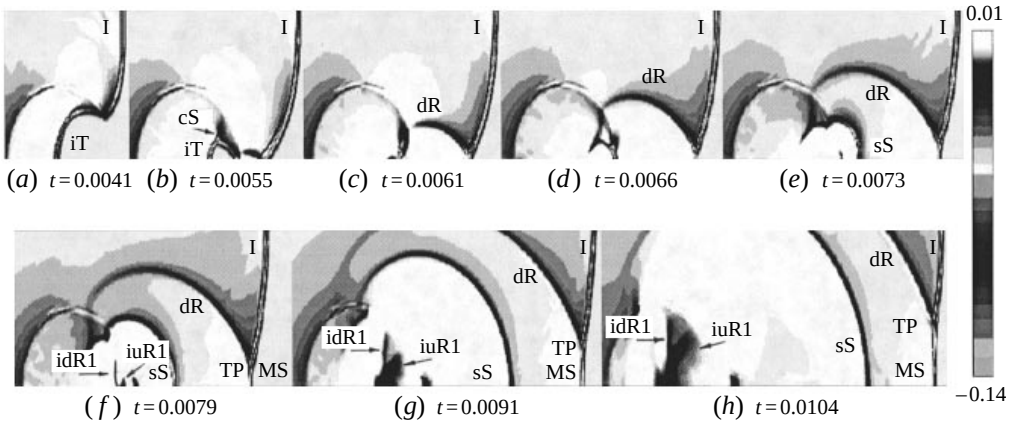

FIGURE 6. $\nabla \cdot \boldsymbol{u}$ patterns for an $M = 1.14$ shock refraction on an air–R12 bubble.

In the third row the incident wave curves around the back side of the bubble, and maintains a near-normal intersection with the bubble surface, a phenomenon first emphasized by Samtaney & Zabusky (1994). Not clearly seen in this figure is the wave behaviour upstream of the bubble and the interior transmitted shock interaction, which we will discuss below.

In row (iv), a closed shock cavity begins to collapse within the bubble. At larger Mach numbers, (*b*)(iv) and (*c*)(iv), the downstream bubble interface is very close to the transmitted wave, that is the internal cavity of unaffected gas has a decreasing volume and increasing surface curvature. Also in (*b*)(iv) and (*c*)(iv) the circulation is sufficiently strong to begin to roll up the interface near its apex, as discussed below.

3.1.1. *Cavity implosion and re-expansion and downstream shock collisions*

We now discuss wave patterns for an $M = 1.14$ shock by examining $\nabla \cdot \boldsymbol{u}$ in figure 6. The collapsing cavity in 6(*b*) has a corner shock, cS, at its highest curvature point, a generic occurrence that is seen more clearly at cases of higher Mach numbers, below. At (*c*) the interior shock cavity has collapsed. In (*d*) and (*e*) the interior cavity expands and collides with the interface and a secondary shock (sS) is transmitted. Note that MS indicates the Mach shock on the downstream side and dR, which emanates eventually from the triple point (TP), is a downstream reflected wave, or alternatively a result of the collision of the separate parts of the incident shock on the downstream side of the bubble. In (*f–h*), we see manifestations of the Haas & Sturtevant (1987) phenomenon where two successive upstream propagating reflected wave fronts, idR1 and iuR1, were found inside the bubble. These fronts are expansion and compression waves, respectively, related to the upstream and the downstream edge of the expanding cavity that have both been reflected from the back side of the bubble. Note, iuR1 catches up to idR1 just before (*f*). This phenomenon is particularly clear in figure 7, the on-axis pressure at four time points in 7(*a*) (corresponding to 6(*b–e*)) and three time points in 7(*b*) (corresponding to 6(*f–h*)). The average position of the front and back sides of the bubbles, FS and BS, are indicated for clarity. The first three times in 7(*a*) show increasing pressure within the cavity during its collapse and the three curves in 7(*b*) show the lower-pressure expansion within the bubble. After these waves reach the front side of the bubble interface, they again focus, as shown in the density plot (see figure 11*g*), and create another upstream transmitted shock (uT_2).

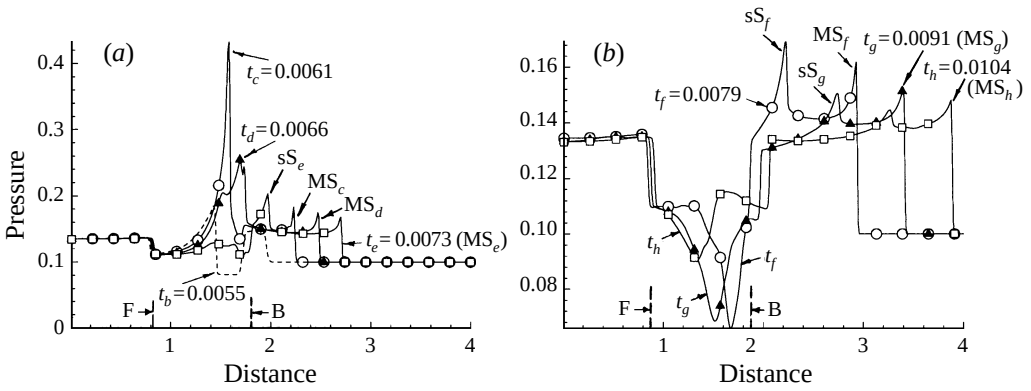

FIGURE 7. Pressure distribution along the x-axis for shock refraction on air–R12 bubble for $M = 1.14$ and an initial bubble radius of 1.0. We see the collapsing and re-expanding cavity and the generation of internal and external waves. B and F are the average positions of the back and front bubble interface, respectively; MS, Mach shock; sS, secondary shock. (*a*) Curves correspond to figure 6(*b*), (*c*), (*d*) and (*e*). (*b*) curves correspond to figure 6(*f*), (g) and (*h*).

Figure 8 shows the space–time diagram of pressure distribution along the x-axis for $M = 1.14$ and 2.5. We see clearly many of the phenomena discussed above. Here, (1) is the location where the shock contacts the front side of the bubble (F) and an (iT) shock is seen within the bubble. At (2) the incident shock (I) first touches the axis on the downstream side of the bubble (the location of the starting point of the secondary shock). The notch to the left of (2) and the yellow-red high-pressure region below it is associated with the collapsing cavity. The width of the notch is the spatial extent of uncollapsed cavity, the yellow-red sS is the downstream secondary shock, and dark-blue dJ is the downstream jet both arising from the interior cavity collapse and will be discussed below. Just below the yellow bifurcation, we see a white expansion region, iR1, which is an interior wave arising from reflection on the back side of the bubble. Next, (3) indicates the location of an upstream jet uJ caused by iR1 focusing near the front side of the bubble. Note that iR2, inside the bubble, results from the reflection of iR1 from the upstream bubble interface. Finally, (4) is location of the starting points for the next downstream and upstream jets.

Note that for the weak incident shock in figure 8(*a*), all the velocities, at the bubble front side, the downstream and upstream jets, are near constant. However, in figure 8(*b*), the upstream interface, F, moves with a non-constant velocity, associated with the bubble oscillation during shock passage, as seen in figures 13 and 14 where one observes variations in bubble volume. The sS overtakes the I, an effect more clearly seen at higher Mach number, as discussed below. Note the upstream transmitted waves uT_1 and uT_2.

We next study the cavity implosion phenomena and downstream coherent shock patterns for $M = 2.5$ and 5.0 in figures 9(*a–f*) and 9(*g–i*), respectively. The white regions are expansions, i.e. positive dilitation. In 9(*a*), although we are beyond the early phase, a finite cavity still exists. The dominating feature in figure 9(*a*, *b*) is the four-shock interaction associated the collapsing cavity. Here T and dT are the inner transmitted shock and its (inner) downstream component, separated by a sharp kink, from which two shocklets emanate. The other dominating features in figure 9(*a–c*) are the r-directed shock wave (which arises from the collision of the curved I shock waves on the bubble back side) and the Mach disk. Below we show that a strong

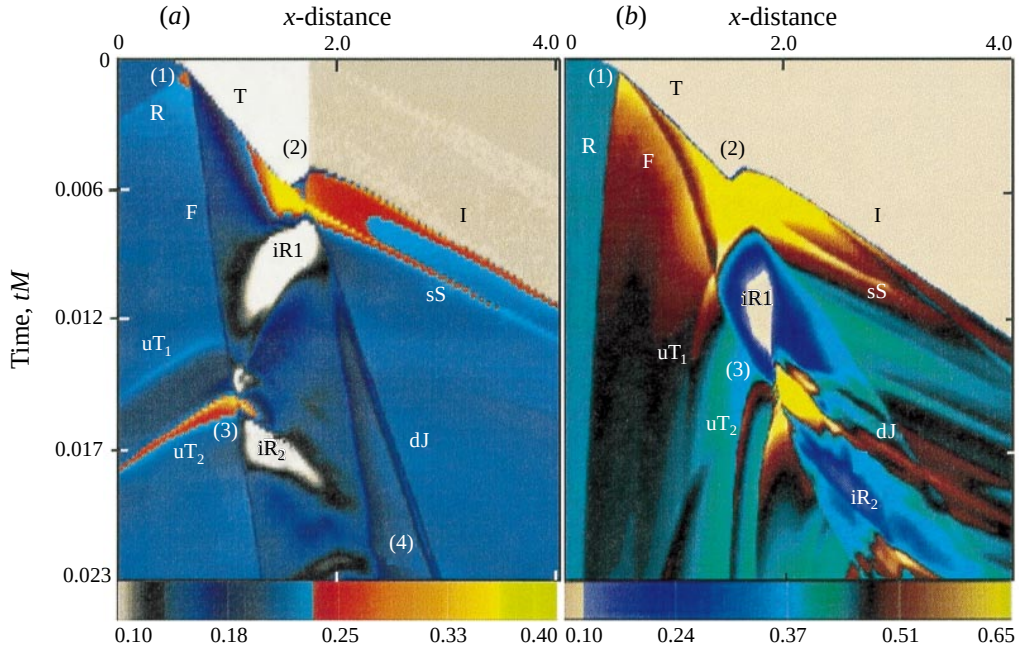

FIGURE 8. Space–time diagram of on-axis pressure, where the horizontal axis is normalized distance $r_0 = 1$ and the vertical axis is normalized time, tM. (*a*) $M = 1.14$, (*b*) $M = 2.5$.

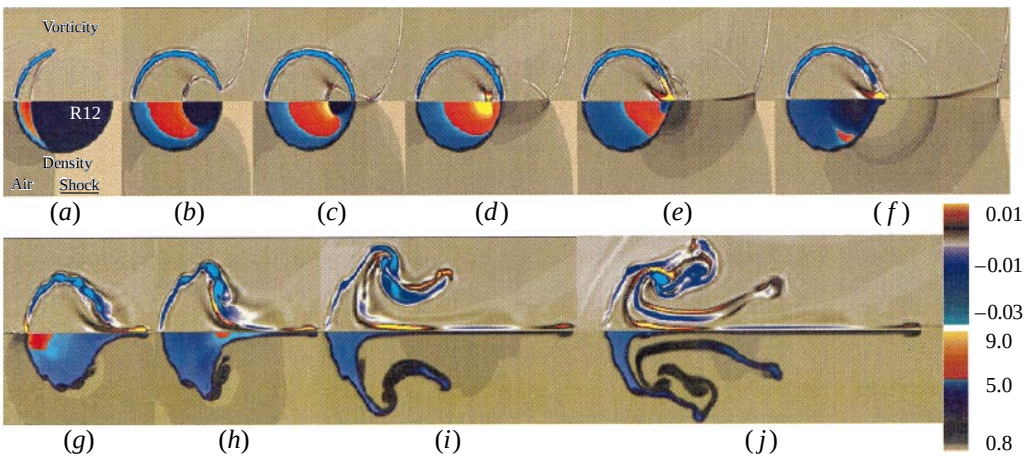

FIGURE 11. Vorticity (upper) and density (lower) for an $M = 1.14$ shock interacting with a R12 bubble at normalized times: (*a*) $t = 0.0042$, (*b*) $t = 0.0048$, (*c*) $t = 0.0055$, (*d*) $t = 0.0061$, (*e*) $t = 0.0062$, (*f*) $t = 0.0085$, (*g*) $t = 0.0152$, (*h*) $t = 0.0238$, (*i*) $t = 0.0498$, (*j*) $t = 0.0693$.

shear layer arises behind the Mach disk. Also in figure 9(*c*), the 'secondary shock' (sS) develops from the expanding cavity, and we track this feature in all subsequent frames. It overtakes the I shock in figure 9(*f*) (Mach 2.5).

Very similar phenomena occur for $M = 5.0$. In figure 9(*g–i*) we show the $\nabla \cdot \boldsymbol{u}$ for $tM = 0.0054$, 0.0079 and 0.0132 which corresponds closely to figure 9(*a,d,f*). An upstream transmitted shock (uT_1) arises from the interaction between the shocklet and the interface in figure 9(*g*). It overtakes R on the upstream side, as shown in

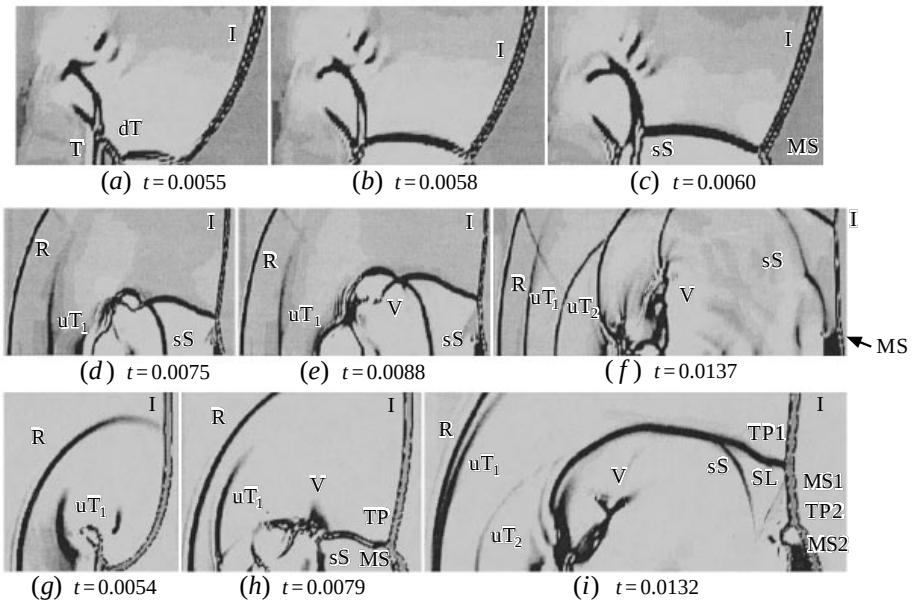

FIGURE 9. $\nabla \cdot \boldsymbol{u}$ patterns for shocks interacting with an R12 bubble, (*a–f*), $M = 2.5$, (*g–i*), $M = 5.0$.

figure 9(*i*). Also, we see a 'Complex Mach Reflection' which has a triple point (TP) in figure 9(*h*), and a 'Double Mach Reflection' which has two triple points (TP1) and (TP2) in figure 9(*i*). Here, SL is the primary slipline (or shear layer). In figure 9(*d–f*) the *r*-directed shock interacts with the density interface and has a large influence on vorticity generation, as discussed later.

The timing and magnitude of these events are shown in the maximum pressure and temperature diagrams at three Mach numbers in figure 10(*a*, *b*). For the pressure the two highest Mach numbers show two strong peaks, which correspond to the collapse of the interior cavity within the bubble. For $M = 5$ the maximum value of the pressure during the first bubble collapse is about six times higher than initial pressure. The temperature signals in figure 10(*b*) have a similar behaviour.

These phenomena are very rapid and associated with large compressions during collapse. In real fluid flows, the peaks will be affected by dissipation and thermal conductivity effects, which have been ignored in this work. An optimization question for future study is: what combination of physical and geometric parameters will lead to a maximum amplification of pressure and temperature? We note that the magnitude of the pressure enhancement is quantitatively different from the case of a shock crossing a bubble in liquid (Ding & Gracewski 1995) which arises from a different equation of the state.

3.2. *Circulation deposition and scaling*

Let us examine the vorticity/density (upper/lower) sequences in figures 11, 13 and 14, corresponding to $M = 1.14$, 2.5, 5.0. In figure 11(*a*, *b*) (see p. 338) the incident shock is in contact with the bubble and in the later frames it interacts with itself as it moves downstream. The interfacial layer of vorticity is essentially undisturbed in frames (*a–c*) and begins to roll-up in (*d–g*). The cavity collapses in (*d*) and an expansion is evident in (*e*). This is accompanied by upstream and downstream signals in density

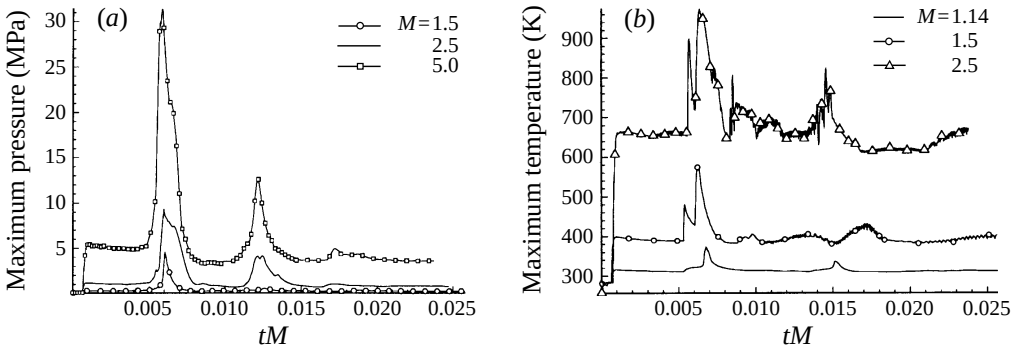

FIGURE 10. Maximum magnitudes of (*a*) pressures (MPa), (*b*) temperatures (K) vs normalized time tM.

and pressure (which we have discussed). The outer wave structures are interacting with the backside bubble interface and corresponding vortex layers in (*d*) and (*e*).

As the interface begins to roll up positive (red-yellow) vorticity always appears. This vorticity is generated by 'baroclinic processes', whose density gradient is associated with the interface. The scaling of this phenomenon is under investigation. In (*e*) and (*f*), we see a downstream jet (dJ) issuing from the bubble which becomes progressively weaker in (*g–j*). Moreover, a small transient upstream jet (uJ) is apparent in (*g*).

These features are clearly seen in the integrated vorticity space-time diagram, figures 12(*a*) and 12(*b*) which show the integrated net and positive vorticity, respectively. At (1) the shock first interacts with the bubble and the most gradual sloping line indicates the incident shock (I) in both diagrams. The transmitted shock generates positive (blue in *b*) vorticity as it straightens. At (2), the cavity collapses and produces a downstream jet (dJ), indicated by the red domain in (*a*) and the red-yellow-dark blue domain in (*b*). The striated black regions moving toward the right (V) are indicative of roll-up and vortices merge at (3). This is accompanied by strong baroclinic effects along the high density gradients, for in 12(*a*) we see a small red-yellow region to the left of the blue region. This corresponds to figure 11(*h*) at $t = 0.0238$. In this case the positive vorticity is due to the the interaction between the backside interface and the interior wave reflected from the front side of the bubble. In 12(*a*) the second blue region (4) at $tM = 0.05$ arises when the extended negative vortex structure has made another half a rotation. When the internal wave hits the upstream side we see an 'upstream' jet (uJ), a very weak event. Many of the structures have dimensions corresponding to the interfacial layer thickness (about three grid lengths). Thus, for times after that corresponding to figure 11(*h*), our results provide only heuristic guidance for the emerging turbulent mixing.

Figures 13 and 14 show similar quantities at $M = 2.5$ and 5.0. Here we see an asymmetrical deposition of primary negative vorticity (more on the downstream side) and its 'separation' from the bubble interface at (*d–f*). Also seen at (*f*) is the appearance of the primary downstream vortex ring. Note the downstream ring has more fine structure in figure 14. At $M = 2.5$ and 5.0 a new phenomenon is evident near the apex of the bubble, namely a 'complex' vortex ring, or 'vortical projectile'. Its positive vorticity arises mainly from the upward going r-directed shock wave that interacts with the downstream bubble interface. The net result is a diffuse complex three-vortex region configuration which binds and begins to move upward and to the right in figures 13(*h, i*) and 14(*i–k*). Figure 15 (p. 341) shows the vorticity in the $M = 2.5$ case.

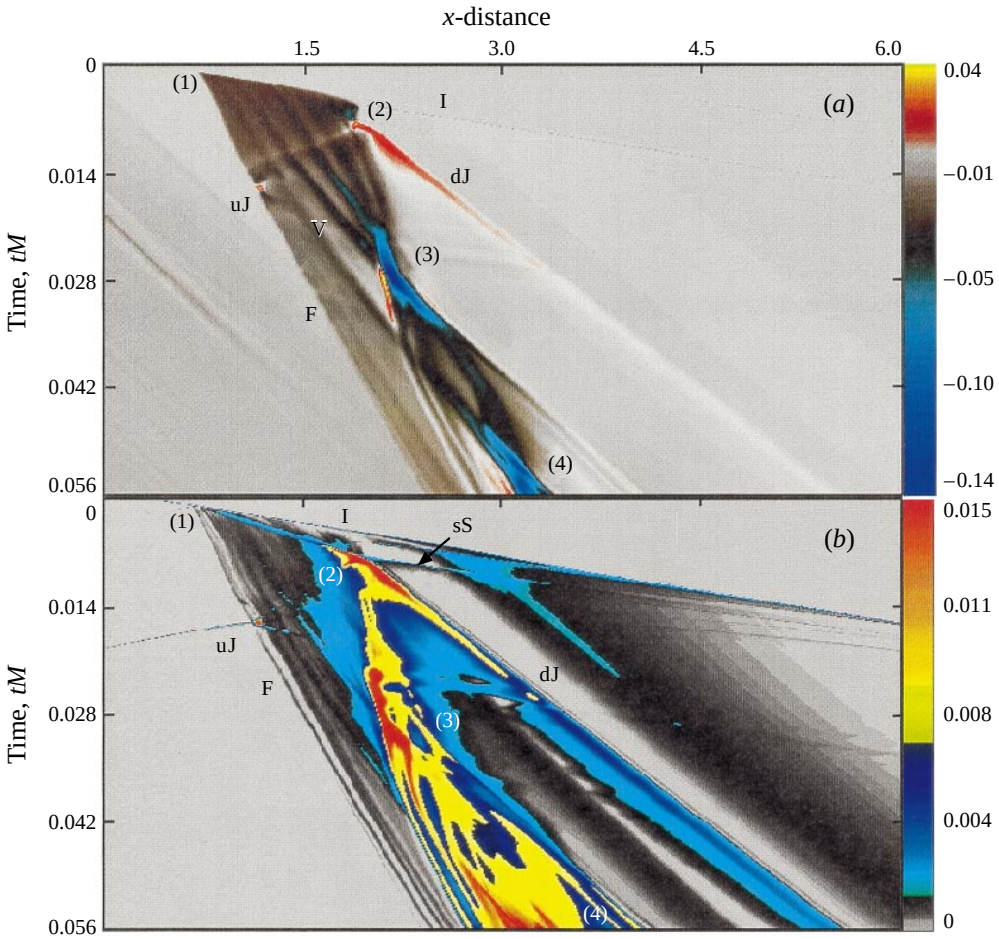

FIGURE 12. Space–time diagram of the r-integrated vorticity for a $M = 1.14$ shock interacting with an R12 bubble. Upper is net vorticity. Lower is positive vorticity. (Space is normalized by the bubble radius and normalized time is indicated.)

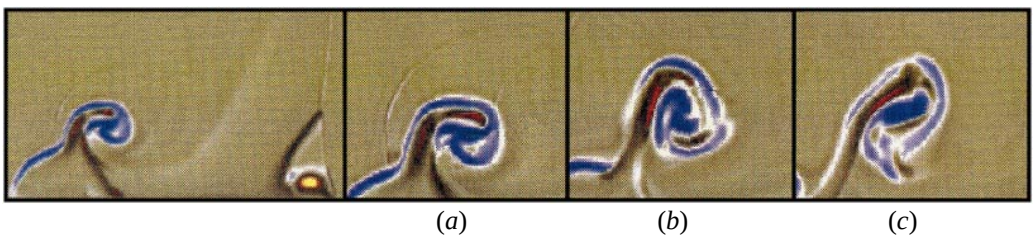

FIGURE 15. Vorticity $M = 2.5$. The left-hand frame is the colour version of figure 13(h); (a–c) are zooms of the vorticity near the apex of the bubble where a vortical projectile is forming. (a) and (c) correspond to figures 13(h) and 13(i).

Figure 16 shows the space–time diagram for the net circulation for $M = 2.5$ and 5.0. The downstream supersonic vortex ring (dVR) associated with the downstream jet is a persistent feature. The delay or eruption time for the generation of the downstream vortex ring that we mentioned above is seen at (2) in figure 16.

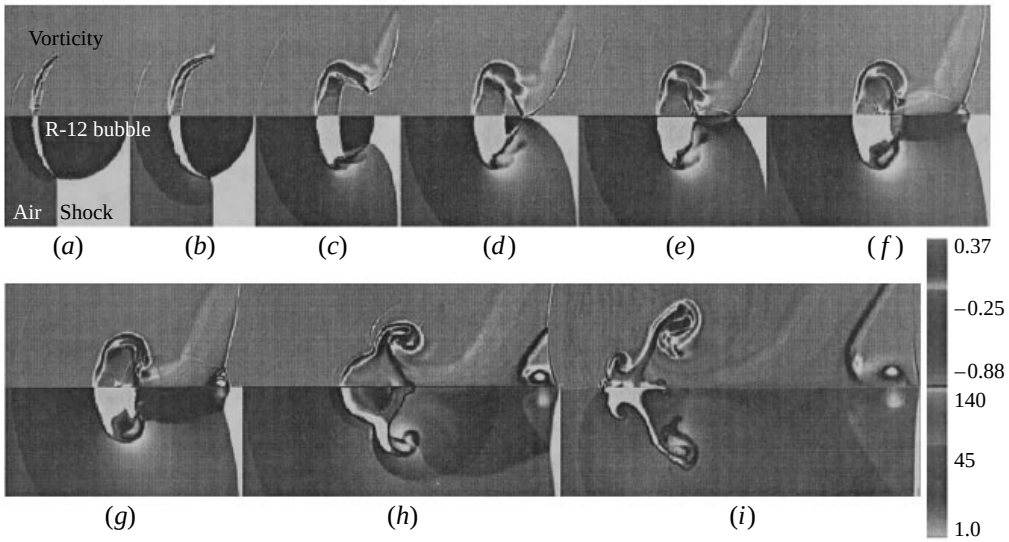

FIGURE 13. Vorticity (upper) and density (lower) for an $M = 2.5$ shock interacting with a R12 bubble at normalized times: (*a*) $t = 0.0019$, (*b*) $t = 0.0029$, (*c*) $t = 0.0045$, (*d*) $t = 0.0053$, (*e*) $t = 0.0057$, (*f*) $t = 0.0065$, (*g*) $t = 0.0070$, (*h*) $t = 0.0094$, (*i*) $t = 0.098$.

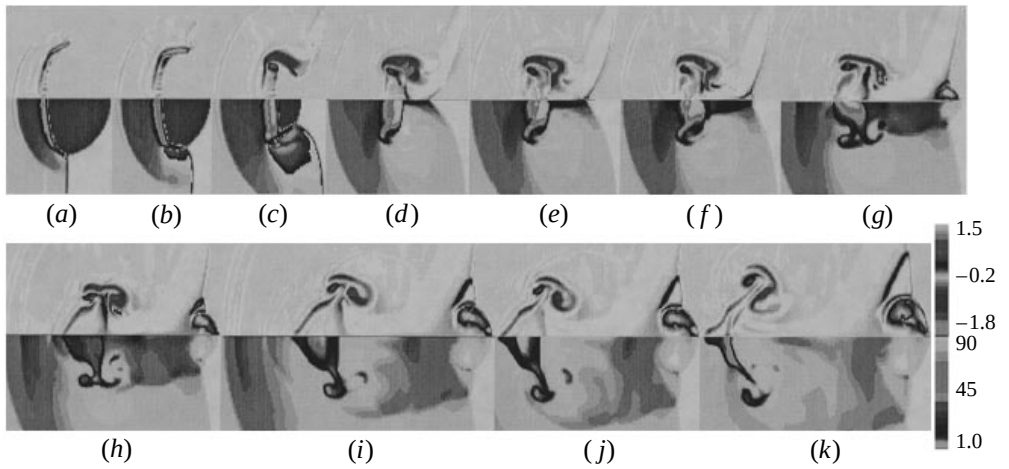

FIGURE 14. Vorticity (upper) and density (lower) for an $M = 5.0$ shock interacting with an R12 bubble at normalized times: (*a*) $t = 0.0024$, (*b*) $t = 0.0032$, (*c*) $t = 0.0045$, (*d*) $t = 0.0057$, (*e*) $t = 0.0062$, (*f*) $t = 0.0066$, (*g*) $t = 0.0078$, (*h*) $t = 0.0093$, (*i*) $t = 0.0108$, (*j*) $t = 0.01\,14$, (*k*) $t = 0.0132$.

Figure 17 quantifies the positive, negative and net circulations (or integrated vorticity) in various spatial domains. These computed circulations are normalized by the circulation deposited on the upper-half of the interface as obtained from the scaling formula, (5.12) of Samtaney & Zabusky (1994):

$$\tilde{\Gamma} = \left(1 + \frac{\pi}{2}\right) \frac{2\gamma^{1/2}}{1+\gamma}(1 - \eta^{-1/2})(1 + M^{-1} + 2M^{-2})(M-1) r_0 c_s, \tag{26}$$

where r_0 is the bubble radius and c_s is the ambient speed of sound in air. The integrations for circulations associated with the bubble are obtained by correlating

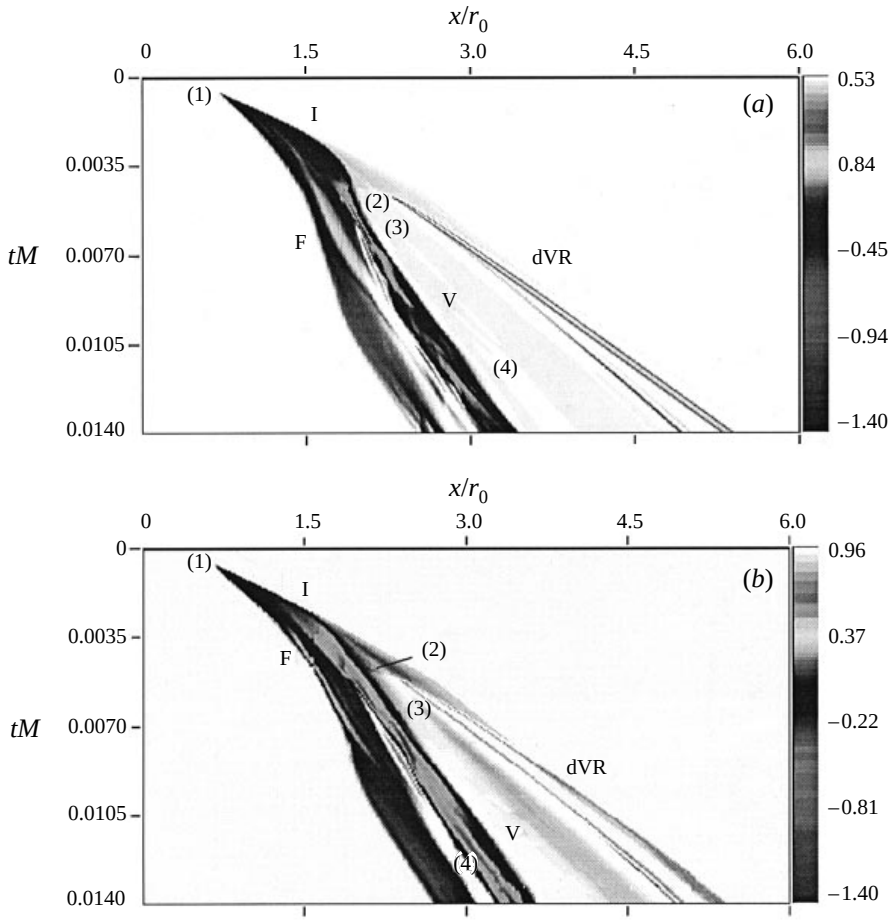

FIGURE 16. Space–time diagram of the r-integrated vorticity: I, incident shock; F, front side of the interface; dVR, downstream vorticity ring; V, vorticity ring on down stream side interface; in (*a*) $M = 2.5$ (*b*) $M = 5.0$.

with the bubble fluid, ρ_2. That is we add the relevant circulation if the density associated with the bubble gas is above some threshold. We can do this because the code is multispecies and treats the bubble fluid separately from the ambient fluid. Similarly, the circulations associated with the vortex ring are obtained by adding all relevant circulations downstream of the right-hand edge of the bubble to the right-hand end of the domain.

First, for $M = 2.5$ and $M = 5.0$, we note that during the initial phase, the results are in excellent agreement because the normalization formula is more accurate at higher Mach numbers. The primary negative circulation grows linearly, then decreases in magnitude and soon begins an increase, an effect observed earlier for shock–cylinder interactions. At low Mach number the secondary positive circulation generated inside the bubble is slightly larger than that generated by the Mach disk and they both approach a constant value. For $M = 5.0$, the slip surface of the Mach disk yields large positive and negative circulations whereas the primary negative circulation associated with the bubble interface has been decreasing slowly.

We conjecture that in three dimensions, with axisymmetry relaxed, one could

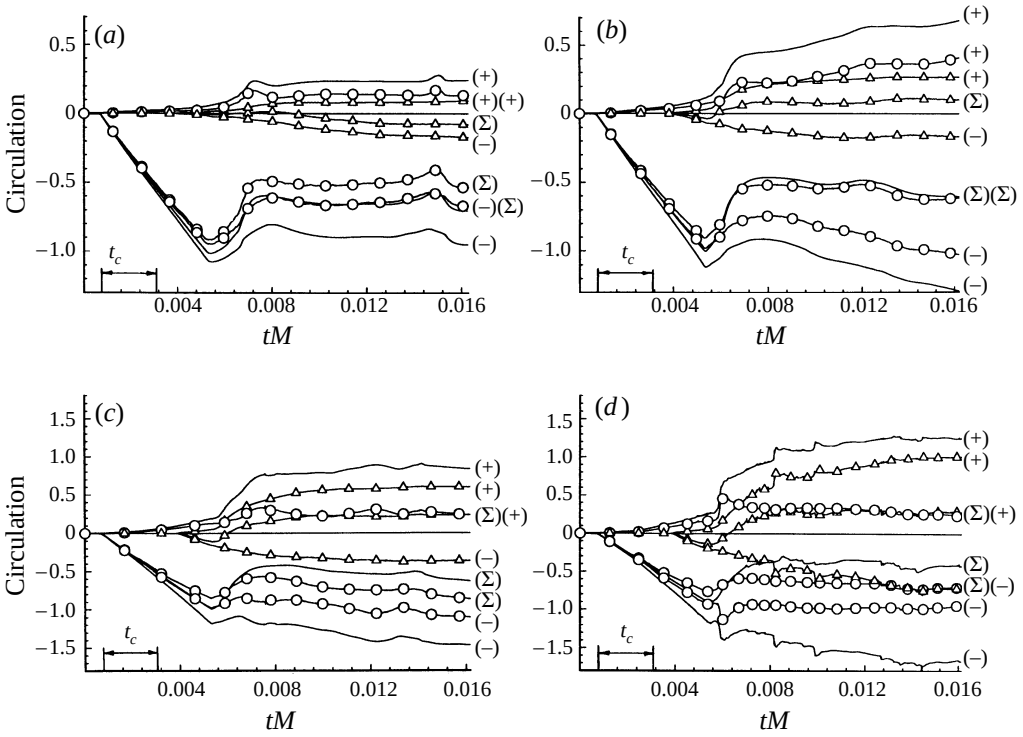

FIGURE 17. Positive (+), negative (−) and net (Σ) circulations normalized by $\widetilde{\Gamma}$ as a function of normalized time (tM) with different Mach numbers. t_c is the time for the shock to traverse $2r_0$. (*a*) $M = 1.14$, (*b*) $M = 1.5$, (*c*) $M = 2.5$, (*d*) $M = 5.0$. (—— circulation in the entire computational domain; –○–○–, circulation inside the bubble; –△–△–, circulation generated by the slip surface of the Mach disk.

have a very complex interaction resulting in multi-directional concentrated jets and vortical projectiles which arise from the vorticity deposited by multi-directional shocks interacting with the evolving bubble interface. These effects should be addressed when turbulent mixing processes are considered in an environment of shocks interacting with many bubbles. We expect to contribute to solving this problem.

4. Discussion and conclusions

In the present work we have used the Harten–Yee TVD scheme to solve the axisymmetric Euler equations for a planar shock and a spherical F/S (R12) bubble for $M \leqslant 5$. We have discussed the wave and vorticity structures associated with collapse and re-expansion of the cavity in the bubble formed by the transmitted shock at several Mach numbers. We have visualized the shock implosion morphologies and quantified vorticity generation. Some interesting points are the following:

(1) All types of the shock configurations, from RR to MR will occur when the shock passes over a bubble (even for a weak, $M = 1.14$ incident shock). Negative vorticity is deposited due to baroclinicity on the F/S interface. For strong shocks the negative vorticity begins to separate from the downstream interface of the bubble.

(2) The interior transmitted shock forms a collapsing cavity. At its point of highest curvature this cavity has a 'triple point' at which a positive vortex layer is created and three transmitted shocks are interacting with each other.

(3) Owing to the interaction of two curved approaching incident shocks on the downstream side of the bubble, an axisymmetric Mach disk occurs on the downstream side of the bubble. A vortex ring arises from these conical vortex layers. The Mach disk grows in a self-similar manner.

(4) On the downstream side, the supersonic jet may overtake the incident shock. A weak transient upstream jet is produced when the interior reflected wave focuses on the front of the interface.

(5) The interior shock wave is reflected between the back and front of the bubble interface, which causes the bubble to oscillate. For a strong shock these interactions modulate the velocity of the smooth front side of the bubbles.

(6) A downstream r-directed shock has a large influence on the generation of a secondary positive vorticity layer on the back side. This vortex layer may be large and can bind with the primary negative circulation to form a diffuse vortex ring or vortical projectile which has a vertical component of velocity that carries it beyond the original apex of the bubble.

We acknowledge many useful conversations with Dr Ravi Samtaney. This work has been made possible by the continuing support of a grant from DOE (Grant No. DE-FG0293ER25179.A000) monitored by Dr. Daniel Hitchcock. Computations were done on the C90 at Pittsburgh Supercomputing Center and SP2 at Cornell Theory Center. We acknowledge the support of Center for Computer Aids for Industrial Productivity at Rutgers University.

REFERENCES

Ben Dor, G. 1992 *Shock Wave Reflection Phenomena.* Springer.

Bitz, F. J. & Zabusky, N. J. 1990 David and Visiometrics: Visualizing, diagnosing and quantifying evolving amorphous objects. *Computers Phys.* Nov.–Dec. 603–614.

Cowperthwiate, N. W. 1992 The interaction of a plane shock and a dense spherical inhomogeneity. *Physica* D **37**, 264–269.

Ding, Z. & Gracewski, S. M. 1995 The behaviour of a gas cavity impacted by a weak or strong shock wave. *J. Fluid Mech.* **309**, 183–209.

Haas, J. F. & Sturtevant, B. 1987 Interaction of weak shock waves with cylindrical and spherical gas inhomogeneities. *J. Fluid Mech.* **181**, 41–76.

Harten, A. 1983 High resolution scheme for hyperbolic conservation laws. *J. Comput. Phys.* **49**, 357–393.

Hirsch, C. 1992 *Numerical Computation of Internal and External Flows*, vol. 2, Chap. 19. John Wiley and Sons.

Klein, R. I., McKee, C. F. & Colella, P. 1994 On the hydrodynamic interaction of shock waves with interstellar clouds. I Nonradiative shocks in small clouds. *Astrophys. J.* **420**, 213–236.

Philpott, M., Smith, A. V., Cowperthwaite, N. W. & Youngs, D. L. 1994 Late-time turbulent mixing of a high density gas bubble in a shocked air flow. ($M_s = 1.14$). In *Proc. 4th Intl Workshop on the Physics of Compressible Turbulent Mixing, 1993*, pp. 366–391. Cambridge University Press.

Picone, M. & Boris, J. 1988 Vorticity generation by shock propogation through bubbles in a gas. *J. Fluid Mech.* **189**, 23–51.

Roe, P. L. 1981 Approximate Riemann solvers, parameter vectors and difference schemes. *J. Comput. Phys.* **43**, 357–372.

Roe, P. L. 1985 Upwind schemes using various formulations of the Euler equations. In *Numerical Methods for the Euler Equations of Fluid Dynamics* (ed. F. Angrand *et al.*). SIAM.

Rudinger, G. & Sommers, L. M. 1960 Behaviour of small regions of gases carried in accelerated gas flows. *J. Fluid Mech.* **7**, 161–176.

Samtaney, R. & Zabusky, N. J. 1993 On shock polar analysis and analytical expressions for vorticity deposition in shock-accelerated density-stratified interfaces. *Phys. Fluids* A **5**, 1285–1287.

Samtaney, R. & Zabusky, N. J. 1994 Circulation deposition on shock-accelerated planar and curved density-stratified interfaces: models and scaling laws. *J. Fluid Mech.* **269**, 45–78.

Winkler, K.-H., Chalmers, J. W., Hodson, N. S. W., Woodward, P. R. & Zabusky, N. J. 1987 A numerical laboratory. *Physics Today* **40** (10), 28–37.

Yee, H. C., Warming, R. F. & Harten, A. 1985 Implicit total variation diminishing (TVD) schemes for steady-state calculations. *J. Comput. Phys.* **57**, 327–360.